

Cite this: *Mater. Adv.*, 2024,
5, 8475

Impact of static and dynamic disorder effects on the charge transport properties of merocyanine single crystals†

Nora Gildemeister,^{‡a} Sven Geller,^{‡a} Robert Herzhoff,^a Fabrizia Negri,^{‡b}
Klaus Meerholz^{*a} and Daniele Fazzi^{‡*ab}

Merocyanines are polar organic π -conjugated molecules consisting of electronic donor (D) and acceptor (A) subunits connected via a conjugated bridge. They have been investigated because of their unique self-assembly and optoelectronic properties, making them ideal active materials for organic electronic applications. The understanding of their charge transport properties at the nanoscale is very challenging and mostly an unexplored field. We report a theoretical study on modelling the hole transport parameters and mobility, together with the investigation of the structure–property relationships of seven merocyanine single crystals, consisting of different combinations of D–A units. We critically discuss the impact of both static (energetic) and dynamic (thermal) disorder effects on charge mobility and transport networks, by emphasizing the importance of including such contributions for an in-depth understanding of the charge transport properties of polar organic semiconductors.

Received 1st July 2024,
Accepted 18th September 2024

DOI: 10.1039/d4ma00669k

rsc.li/materials-advances

Introduction

Merocyanines are polar organic π -conjugated molecules consisting of electron donor (D) and acceptor (A) subunits connected via a methine bridge. They have been studied for their self-assembly and optoelectronic properties, and they have been tested in the field of organic electronics (OE), namely nonlinear optical devices, photorefractivity,^{1,2} photodetectors, organic solar cells (OSCs),³ and organic field effect transistors (OFETs).⁴ Merocyanines are considered as ideal model systems to investigate the dipole–dipole interaction at the molecular scale, allowing the elucidation of both ground and excited state mechanisms governing the response functions in the solid state.⁵ Structure–property relationships were drawn by correlating the self-assembly characteristics with the charge and exciton transfer properties. Würthner *et al.* demonstrated how different D–A units, as well as the length, steric hindrance and flexibility of the lateral groups (*e.g.*, solubilizing alkyl substituents) can remarkably influence the packing in the solid state and consequently the optical response of merocyanines, leading to sharp and well-defined J- or H-bands in the absorption spectrum.⁶

Extensive experimental investigations were also carried out to rationalize the charge transport properties. Seminal contributions by Würthner and Meerholz⁷ highlighted the correlation between the merocyanine molecular packing in single crystals and the charge mobility. For crystals characterized by a hole mobility of $\mu > 0.05 \text{ cm}^2 \text{ V}^{-1} \text{ s}^{-1}$, merocyanines are organized in one-dimensional (1D) columns or 2D brickwork-type architectures.⁴ By optimizing the casting conditions to create extended single-crystalline domains, hole mobilities as high as $2.34 \text{ cm}^2 \text{ V}^{-1} \text{ s}^{-1}$ were measured in a single-crystal organic field effect transistor (SC-OFET), reaching similar performance levels as classical organic semiconductors, such as those based on acenes, naphthalenediimides or oligothiophenes.⁸

In contrast, few theoretical and computational investigations are present in the literature. Engels *et al.* first modelled the intra-molecular charge transport properties of a series of merocyanines, highlighting the impact of the cyanine-like structure in affecting both charge and exciton reorganization energy.⁹ Recently, we reported an extended computational study by modelling the intra- and inter-molecular charge transport (CT) properties of a library of merocyanines consisting of various donor and acceptor groups.⁹ For the CT intra-molecular properties (*e.g.*, internal reorganization energy), we found that constrained density functional theory (C-DFT) is an effective method to describe the ground state bond length alternation (BLA) pattern of merocyanines in condensed phases, leading to hole reorganization energies (λ) of the order of 120–280 meV. Through the evaluation of electronic coupling integrals (J) and

^a Institut für Licht und Materialien, Department für Chemie, Universität zu Köln, Greinstr. 4-6, 50939 Köln, Germany. E-mail: klaus.meerholz@uni-koeln.de

^b Università di Bologna, Dipartimento di Chimica ‘Giacomo Ciamician’, Via P. Gobetti, 85, 40129 Bologna, Italy. E-mail: daniele.fazzi@unibo.it

† Electronic supplementary information (ESI) available. See DOI: <https://doi.org/10.1039/d4ma00669k>

‡ These authors contributed equally to this work.



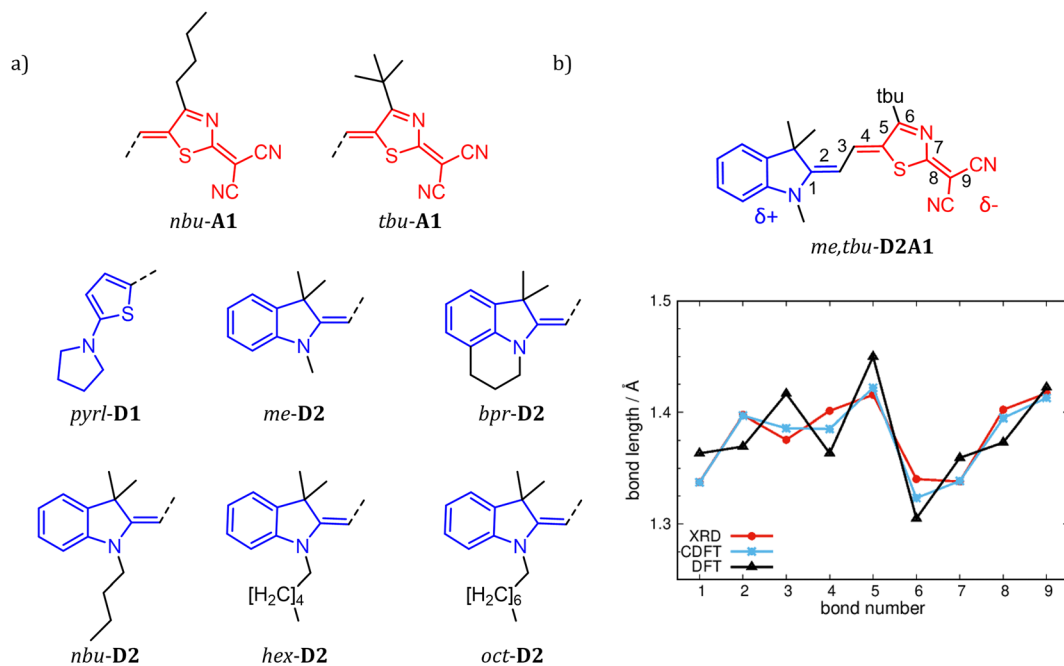


Fig. 1 Chemical structures of R_1 -D1, R_1 -D2 and R_2 -A1 (a), with $R_1 = me-, bpr-, nbu-, hex-, oct-$ and $pyr-$ (blue sketches) and $R_2 = tbu-$ and $nbu-$ (red sketches). (b) BLA path (see bond numbering) exemplary for me,tbu -D2A1. Bond lengths in Å are, respectively, from XRD data⁴ (red line), C-DFT (CAM-B3LYP-D3/6-311G**, gas phase, blue line, $\delta^{D/A} = \pm 0.6q$) and DFT (ω B97X-D/6-311G**, gas phase, black line).

the use of a charge diffusion (hopping) kinetic-Monte Carlo algorithm, we computed the hole mobility for six merocyanine single-crystals belonging to the **D1A1** species (**D1** – 2-aminothiophene and **A1** – 2-(4-alkylthiazol-2(3*H*)-ylidene)malonitrile, see the chemical structure in Fig. 1), and one crystal belonging to the **D2A1** species (**D2** – 1-butyl-3,3-dimethylindolin-2-ylidene ('Fischer base')). In agreement with experimental data, we found that the hole mobility maximizes when the merocyanines are packed in slipped, antiparallel, pairs arranged in 2D interconnected architectures.

The importance of including both static (electrostatic and polarization effects) and dynamic (thermal fluctuations) disorder in the simulations of the charge transport mechanisms of organic semiconductors has been largely documented.^{10–13} Electrostatic and induction effects shift the energy levels of the charge carriers^{14,15} affecting the site energy distribution (ΔE_{ij}) and ultimately the transfer rates (k_{ij}^{eT}) and the mobility.¹⁶ Dynamical effects can induce large fluctuations of the electronic transfer integrals, impacting as well on the transfer rate and charge mobility.^{17–20} The fine interplay between the electronic coupling and the reorganization energy, as quantified by the parameter $\xi = 2|J|/\lambda$, determines the charge transport regime, which can range from adiabatic (band-like, $\xi \geq 1$) to intermediate ($0.2 < \xi < 1$) and non-adiabatic (hopping-like, $\xi \leq 0.2$).^{21–23} Thermal disorder can either enhance the transfer rates opening new transport channels,^{24–26} for cases of highly localized charges (*e.g.*, hopping regimes), or reduce the charge mobility, for cases of delocalized charge carriers (*e.g.*, band or intermediate regimes).^{27,28} Generally, thermally induced fluctuations dynamically localize the charge carrier wave function over few molecular sites on the picosecond time scale, leading to

complex (*e.g.*, polaronic) transport mechanisms.^{17,18,22,29–31} While for classical (non-polar) organic semiconducting systems, such as acenes (*e.g.*, naphthalene, tetracene, pentacene, and rubrene)²⁶ and thioacenes,¹⁸ the impact of disorder effects on the charge transport properties has been well addressed theoretically and experimentally, for strong dipolar compounds such as merocyanines such effects are yet unexplored, and a fundamental understanding is still lacking.

In this investigation, we analyse how static and dynamic disorder effects impact on the charge transport properties of different merocyanines characterized by various **D-A** moieties and furnished with different lateral chains. The latter induce various solid-state packing motifs, ranging from columnar (1D) to brick-wall (2D and 3D) self-assembly. Our findings reveal a detrimental impact of static disorder on the charge mobility, regardless of the nature of the **D-A** groups. At the same time, our simulations show that thermal fluctuations lead to a broadening of the electronic coupling, independent of the **D-A** units and lateral chains. The thermal broadening, as well as the oscillations affecting the charge transfer integrals the most, parallels what was already observed for other organic semiconductors, like acenes^{10,25,32,33} perylene-bis-imide derivatives¹² and thioacenes.³⁴ Finally, we demonstrate how disorder effects change the hole mobility and the charge transport network by affecting its topology.

Methods

Materials

Two species of merocyanines were studied (Fig. 1a). The first (**D1A1**) is composed of a donor unit **D1** (2-aminothiophene)



and an acceptor unit **A1** (2-(4-alkylthiazol-2(3*H*)-ylidene)malonitrile).⁹ The second (**D2A1**) is made by a **D2** (1-butyl-3,3-dimethyl-indolin-2-ylidene ('Fischer base')) group and an **A1** unit (Fig. 1b). To reduce computational costs (as related to the evaluation of the static and dynamic disorder effects), we considered one prototypical species from **D1A1**, namely R_1, R_2 -**D1A1**, with R_1 pyrrolidine (*pyrl*) attached at the donor moiety and R_2 *tert*-butyl attached at the acceptor (*pyrl, tbu-D1A1*). For the **D2A1** species (Fig. 1b), a molecular library was generated by varying the lateral solubility groups attached on **D2** (R_1 -), including methyl (*me*), propyl bridge (*bpr*), *n*-butyl (*nbu*), *n*-hexyl (*hex*) and *n*-octyl (*oct*) alkyl chains, as well as those attached on **A1** (R_2 -), namely *tert*-butyl (*tbu*-) and *n*-butyl (*nbu*-) groups. The six resulting combinations (R_1, R_2 -**D2A1**) are *me, tbu, bpr, tbu-, nbu, tbu-, nbu, nbu-, hex, tbu-,* and *oct, tbu-D2A1*. All six combinations have been previously synthesised by Würthner *et al.* and the experimental data referring to the synthetic procedure and X-ray diffraction analyses can be found in ref. 4, 35 and 36.†

Computational methods

Equilibrium geometries. Density functional theory (DFT) geometry optimization and vibrational frequency calculations were performed with Gaussian16 version C.01³⁷ using the range separated hybrid functional ω B97X-D and the polarized Pople split-valence triple-zeta 6-311G** basis set with polarization functions. Constrained DFT (C-DFT) calculations were performed with NWChem version 6.8,³⁸ using the Coulomb attenuated method CAM-B3LYP with the D3 dispersion correction scheme and the 6-311G** basis set. Neutral ground state calculations were performed at the restricted DFT level, while calculations of the charged states were performed at the spin-polarized unrestricted (UDFT) level.

Charge transport parameters and Brownian charge mobility (absence of static disorder). Internal reorganization energies (λ_i) were computed *via* the adiabatic potential approach (four-point method).^{39,40} Charge transfer integrals ($J_{ij} = \langle \psi_i | \hat{H} | \psi_j \rangle$, where ψ is the molecular orbital wave function on site ij and \hat{H} is the dimer electronic Hamiltonian) were computed both at the DFT (ω B97X-D/6-311G**) and at the semi-empirical ZINDO/S⁴¹ levels, according to the dimer projection method (DIPRO).^{42,43} A network analysis to map the transfer integrals of each crystal was carried out *via* the python package NetworkX (see the ESI,† Fig. S9).⁴⁴ Transfer rates between sites k_{ij}^{eT} were calculated using the semiclassical Marcus formulation:^{45,46}

$$k_{ij}^{eT} = \frac{2\pi J_{ij}^2}{\hbar} \frac{1}{\sqrt{4\pi\lambda k_B T}} \exp\left(-\frac{(\Delta E_{ij} + \lambda)^2}{4\lambda k_B T}\right) \quad (1)$$

where λ is the total reorganization energy as the sum of the internal and external contributions ($\lambda_i + \lambda_o$), in which λ_o is set to 0.05 eV,^{9,47,48} ΔE_{ij} is the site energy difference, k_B is the Boltzmann constant and T is the temperature. λ_o is conservatively set to 0.05 eV, reflecting the value explicitly computed in our previous study by using a C-DFT supra-molecular approach as applied to *pyrl, tbu-D1A1*.⁹ Such a value is about the same

order of magnitude as those reported in other investigations, in which λ_o was instead evaluated *via* quantum mechanics/molecular mechanics (QM/MM) approaches based on polarizable force fields.^{48–50}

Charge carrier mobilities (μ), in the absence of static energetic disorder ($\Delta E_{ij} = 0$), were computed for each single crystal of R_1, R_2 -**D2A1** (see the Materials section) *via* kinetic Monte-Carlo (kMC) simulations considering the Brownian diffusion scheme and calculating the diffusion coefficient D with a multiple set of kMC trajectories.^{19,20,51} An approximate linear dependence of the mean square displacement (MSD) of the charge $[r(t) - r(0)]^2$ as a function of time t was obtained by averaging over the subsets of 1000 kMC trajectories. The diffusion coefficient D was obtained from the fitted linear dependence of the MSD:

$$D = \lim_{t \rightarrow \infty} \left(\frac{\text{MSD}}{6t} \right) \quad (2)$$

The charge mobility (μ) was finally computed by the Einstein–Smoluchowski equation:

$$\mu = \frac{eD}{k_B T} \quad (3)$$

Static disorder. Electrostatic and induction effects were evaluated for all compounds (ESI,† Fig. S10), considering supercells containing each 512 molecules. Supercells were constructed, so that their extension (*i.e.*, the number of molecules per each crystallographic axis) was the same. This procedure resulted in an $8 \times 8 \times 4$ supercell of *pyrl, tbu-D1A1* (2 molecules in a unit cell), a $4 \times 4 \times 8$ supercell of *me, tbu-D2A1* (4 molecules in a unit cell), a $4 \times 8 \times 4$ supercell of *bpr, tbu-D2A1* (4 molecules in a unit cell), an $8 \times 8 \times 4$ supercell of *nbu, tbu-* (2 molecules in a unit cell), a $4 \times 8 \times 4$ supercell of *nbu, nbu-* (2 molecules in a unit cell), an $8 \times 4 \times 4$ supercell of *hex, tbu-* (4 molecules in a unit cell) and an $8 \times 4 \times 8$ supercell of *oct, tbu-D2A1* (2 molecules in a unit cell). The static disorder parameters were computed as implemented in the program package VOTCA^{42,51} and partial charges were computed *via* DFT calculations (ORCA version 5.0.1)⁵² based on the CHELPG scheme at the ω B97X-D3/6-311G* level of theory. Site energies (E_i^{el}) are evaluated from partial charges of neutral (q^n) and charged (q^c) molecules:^{53,54}

$$E_i^{\text{el}} = \frac{1}{4\pi\epsilon_0} \sum_{a_i} \sum_{\substack{b_k \\ k \neq i}} \left(\frac{q_{a_i}^c - q_{a_i}^n}{\epsilon_s r_{a_i b_k}} \right) q_{b_k}^n \quad (4)$$

where $r_{a_i b_k} = |r_{a_i} - r_{b_k}|$ is the distance between atoms a_i (referring to molecule i) and b_k (referring to molecule $k \neq i$), and ϵ_s is the static relative dielectric constant. Polarization contributions are computed explicitly and included in ϵ_s . Such effects are modelled *via* a polarizable force field based on the Thole model⁵⁵ (as implemented in VOTCA) where multipolar contributions are refined *via* an iterative procedure based on the evaluation of the induced dipole moments and polarizabilities.

† CCDC 2004947 contains the supplementary crystallographic data of *oct, tbu-D2A1* measured by Murrey *et al.*³⁶



Thermal disorder. Thermal effects were computed for a subset of R_1, R_2 -D2A1, namely *me,tbu-* and *nbu,tbu-D2A1*, and for *pyrl,tbu-D1A1*. Rigid molecular dynamics (MD) simulations were performed *via* GROMACS⁵⁶ on supercells of *me,tbu-*, *nbu,tbu-D2A1* and *pyrl,tbu-D1A1*. Bonded and non-bonded (*e.g.*, van der Waals) parameters were taken from the OPLS-AA force field.^{57,58} Partial charges were evaluated following the CHELPG scheme on top of the XRD geometries, at the ω B97X-D3/6-311G* DFT level of theory by using ORCA 5.0.1.^{52–54} For MD rigid body approximation, bonds were partially constrained (LINCS algorithm) and angles, dihedrals and impropers were restrained in terms of maximal force constants.¹² After energy minimisation, all systems were equilibrated in the NVT ensemble at 300 K for 1 ns. Equilibration was reached for each system after *circa* 100–300 ps, where the total energy of the system gets stabilized and the RMSD of the atomic positions with respect to the XRD structure is around 10^{-2} nm. The Nosé–Hoover thermostat was used with a time constant of 0.2 ps. The MD integration time step (leap-frog integrator) was 1 fs. For the Coulomb interactions, the particle mesh Ewald for long-range electrostatics method was used, and the van-der-Waals and Coulomb cut-offs were set to 1.0 nm. After the equilibration phase, snapshots of dimers were sampled every 30 fs for a total simulation time of 21 ps for both cases of D2A1, and up to 100 ps for *pyrl,tbu-D1A1*. For each snapshot, the transfer integrals J_{ij} were computed by applying the DIPRO method at the ZINDO/S level.^{42,43} Finally, the Fourier Transform (FT) of the electronic coupling autocorrelation function was computed^{10,12,59} to determine the phonon frequencies affecting the fluctuation of the transfer integrals the most.

Results and discussion

Single molecule analysis: neutral equilibrium structures and intra-molecular reorganization energy

The coupling between the D–A units in merocyanines leads to intra-molecular charge transfer resulting in equilibrium molecular geometries that can be described by a linear combination of polyenic (neutral) and zwitterionic (charge transfer) structures.⁶⁰ A correct description of both ground and excited state geometries challenges the majority of the standard quantum chemical approaches.^{9,61–64} In earlier work, we have shown that by tuning the ground state electronic partial charges, as localized on the donor (δ^D) and acceptor (δ^A) groups by applying the C-DFT methodology, optimized geometries (in a vacuum) reproduce the solid state experimental (XRD) bond length alternation (BLA) patterns. A best match between C-DFT and XRD molecular structures was found for a partial charge of $\delta^{D/A} = \pm 0.6q$, which has been applied throughout this study as well.⁹ The experimental BLA pattern, as shown exemplary for *me,tbu-D2A1* in Fig. 1b, is reproduced by our C-DFT calculations and in line with previous findings.⁹ The BLA patterns of all R_1, R_2 -D2A1 are shown in the ESI,[†] Fig. S1. The BLA parameter, d_{BLA} , defined as the difference between the average single- and double-bond lengths

$$\left(d_{\text{BLA}} = \frac{\sum_i (R_{\text{single}}^i)}{N} - \frac{\sum_j (R_{\text{double}}^j)}{M} \right),$$

ranges between -0.009 \AA (*me,tbu-* and *nbu,nbu-*) and 0.001 \AA (*nbu,tbu-*), indicating for all molecules a quasi-cyanine structure ($d_{\text{BLA}} = 0.000 \text{ \AA}$) in the solid state. The computed C-DFT d_{BLA} values range between 0.002 \AA (*nbu,tbu-* and *oct,tbu-*) and 0.005 \AA (*nbu,nbu-*), in good accordance with the experimental data (ESI,[†] Fig. S1 and Table S1). C-DFT calculations can best predict the single molecule bond length alternations in the solid state,⁹ as shown in Fig. 1b (blue lines), whereas the BLA pattern obtained by DFT gas phase calculations (black lines) cannot reproduce the XRD data (red lines). Indeed, the d_{BLA} value as obtained by DFT for *me,tbu-* is with 0.049 \AA significantly higher than the XRD (-0.009 \AA) and C-DFT (0.004 \AA) d_{BLA} values.

Upon charging the molecule (*i.e.*, oxidation or formation of holes), the BLA changes (ESI,[†] Table S1). Such a structural variation impacts on the intra-molecular charge reorganization energy (λ_i) and, therefore, for a quantitative evaluation of λ_i , it is of utmost importance to correctly assess the BLA for both neutral and charged ground states. The computed (hole) reorganization energies range from 167 meV (*me,tbu-* and *nbu,nbu-*) to 179 meV (*bpr,tbu-*) (ESI,[†] Table S2) and are in agreement with previous findings.⁹

XRD structural analysis and electronic couplings of single crystals

Structural analysis. All six R_1, R_2 -D2A1 compounds show 2D brick-wall structures in which molecules assume an antiparallel slipped configuration, forming mono-dimensional columns (Fig. 2). Within a column (intra-columnar), the acceptor moieties of neighbouring molecules overlap. Depending on the amount of sliding between molecules, as caused by the bulky groups on A and D,⁹ interactions between neighbouring columns (inter-columnar) can be established, thus creating 2D layer packing. As documented by Würthner *et al.*,⁴ for some cases, the donor units of molecules belonging to neighbouring columns overlap as well. Such inter-columnar donor–donor (DD) contacts are present in the single crystals of *me,tbu-*, *bpr,tbu-* and *hex,tbu-*, whereas it is not the case for *nbu,tbu-*, *nbu,nbu-* and *oct,tbu-*. For all cases, the neighbouring columns are aligned parallel to each other, except for *me,tbu-*, where they are rotated by 90° (Fig. S2–S7, ESI[†]). Depending on the type of lateral chains attached on D2 ($R_1 = me-, bpr-, nbu-, hex-$ and *oct-*), the intra-columnar contacts between the acceptor groups of different molecules (AA) can vary in distance, leading to asymmetric charge transfer integrals (*vide infra*).⁹

Electronic coupling analysis. High electronic couplings can occur both amongst merocyanines stacked within a column (intra-columnar transport) and between molecules belonging to neighbouring columns (inter-columnar transport). For the latter, the inter-columnar couplings are mainly in two directions, involving molecules displaced along the long molecular axis as well as along the short molecular axis. Most significant transfer integrals and respective molecular dimers are depicted in Table 1 and Fig. 2.



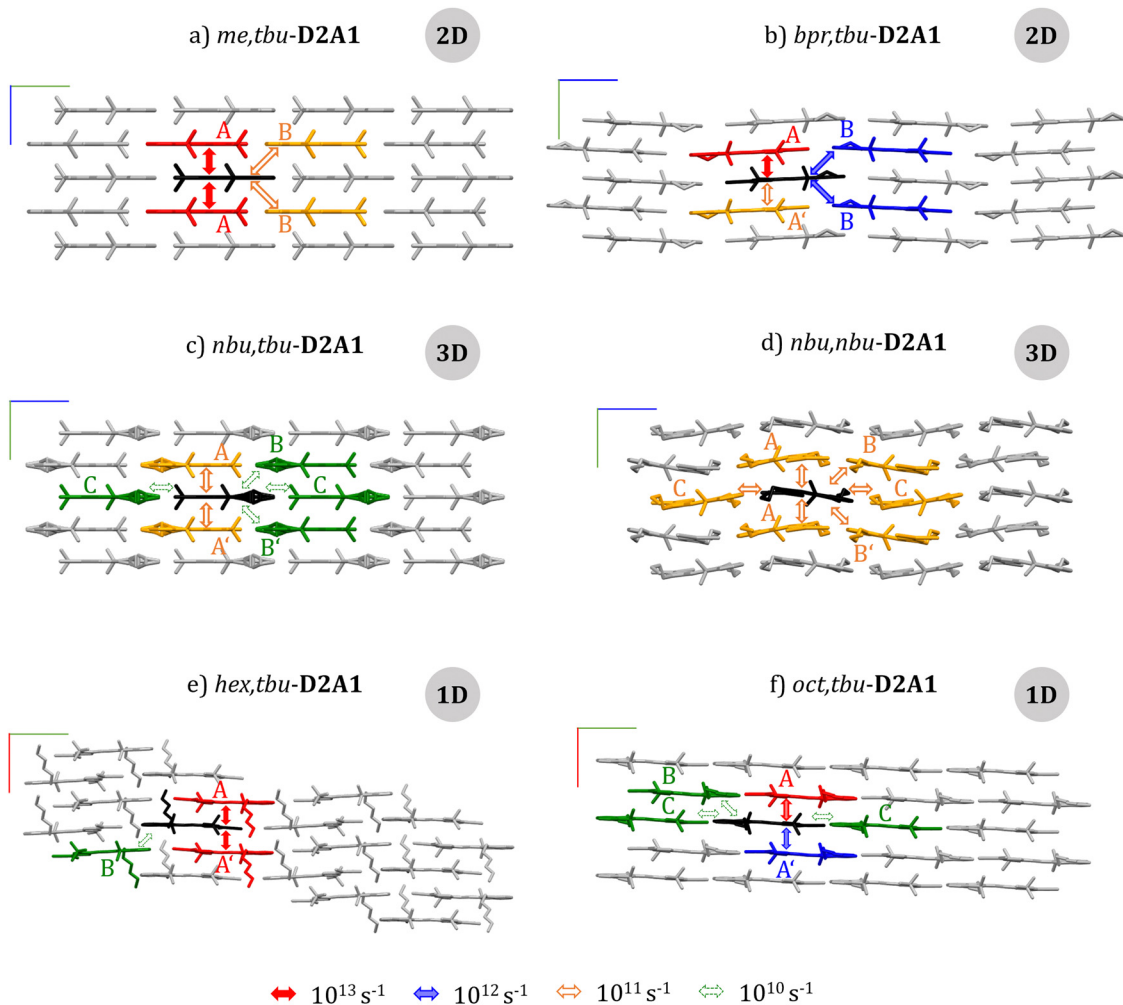


Fig. 2 Side view (a – *me,tbu-*, b – *bpr,tbu-*, c – *nbu,tbu-*, d – *nbu,nbu-*, e – *hex,tbu-*, f – *oct,tbu-D2A1*) onto the long axis of the molecules. For each crystal, a schematic view of the charge transport pathways from the central molecule (black) to the nearest neighbour molecule (red, blue, orange, and green) is reported, with arrows showing the magnitude of the transfer rate (the colour code at the bottom). Cartesian axes of the unit cell: *x* (red), *y* (green) and *z* (blue). The topology of the charge transport network is indicated in grey circles (see the text and the ESI† for the network analysis).

The highest J_{ij} is along the intra-columnar direction with values ranging from 6 meV (*nbu,nbu-*) up to 80 meV (*oct,tbu-*). For *me,tbu-* and *nbu,nbu-*, all intra-columnar transfer integrals are symmetric. For other cases, transfer integrals are asymmetric due to different distances between the $\pi\pi$ -planes as induced by longer alkyl chains (see couplings A and A' in Table 1 and Fig. 2b, c, e and f).

By considering merocyanines displaced along the long molecular axis, the inter-columnar transfer integrals are small (<10 meV) for each species, except for *me,tbu-* and *bpr,tbu-*, showing values of 14 and 16 meV, respectively (dimer B, Table 1 and Fig. 2a and b). The same holds for inter-columnar couplings considering dimers displaced along the short axis, for which the coupling integrals are below 4 meV for all species (Fig. S2–S7 and Tables S3–S8, ESI†). Following the electronic coupling calculations, we classify the interactions as strong ($J_{ij} > 50$ meV), medium ($J_{ij} = 10$ –40 meV) and weak ($J_{ij} < 10$ meV) and analyse them with respect to different crystal directions. When couplings are non-equivalent (A and A' in Table 1)

for consecutive pathways along a specific direction (e.g., within a 1D column), we call these situations asymmetric. Furthermore, a network analysis of the transfer integrals for each crystal of R_1,R_2 -D2A1 was performed and is reported in the ESI† (Fig. S9). Such analysis can anticipate the topology charge transport would assume in the absence of disorder: 1D transport network is predicted for *hex,tbu-* and *oct,tbu-*, 2D transport network for *me,tbu-* and *bpr,tbu-*, and 3D transport network for *nbu,nbu-* and *nbu,tbu-D2A1*. The 3D transport networks for the latter species result from a balance between the intra-columnar hops and the large inter-columnar charge displacements, overall yielding an isotropic charge transport.

Kinetic Monte Carlo Brownian charge mobility: absence of disorder effects

Brownian kMC simulations were performed to evaluate the hole diffusion trajectories of all six R_1,R_2 -D2A1 merocyanine single crystals. Fig. 3 shows the hole spatial displacements resulting from the kMC simulations along with different



Table 1 DFT (ω B97X-D/6-311G**) charge transfer integrals J_{ij} (meV) and rates k_{eT} (s^{-1}) for intra- and inter-columnar dimers of **D2A1**. k_{eT} evaluated according to the semi-classical Marcus theory in the absence of energetic disorder ($\Delta E_{ij} = 0$). The center of mass distances d_{COM} (Å) according to the experimental crystallographic data (XRD)

R_1, R_2^-	Intra-columnar				Inter-columnar			
	Dimer	d_{COM} (Å)	J_{ij} (meV)	k_{eT} (s^{-1})	Dimer	d_{COM} (Å)	J_{ij} (meV)	k_{eT} (s^{-1})
<i>me,tbu-</i> <i>bpr,tbu-</i>	A	6.164	59	1.5×10^{13}	B	10.746	14	8.9×10^{11}
	A	6.447	34	4.4×10^{13}	B	12.635	16	1.0×10^{12}
	A'	6.791	8	2.4×10^{11}				
<i>nbu,tbu-</i>	A	6.264	16	1.0×10^{12}	B	11.108	2	2.1×10^{10}
	A'	6.255	11	4.9×10^{11}	B'	11.113	4	5.0×10^{10}
<i>nbu,nbu-</i>					C	14.782	3	3.6×10^{10}
	A	6.293	6	1.5×10^{11}	B	10.485	8	2.7×10^{11}
					B'	9.955	6	1.3×10^{11}
					C	13.499	6	1.3×10^{11}
<i>hex,tbu-</i>	A	6.322	46	1.5×10^{13}	B	10.833	3	2.6×10^{10}
	A'	6.650	64	2.9×10^{13}				
<i>oct,tbu-</i>	A	6.676	80	2.6×10^{13}	B	9.946	4	5.7×10^{10}
	A'	6.919	31	3.8×10^{12}	C	14.893	3	3.5×10^{10}

Cartesian planes. For an easier comparison, the planes are ordered as the (i) side view onto the long axis of the molecules (corresponding to the view in Fig. 2), (ii) top view, and (iii) side view onto the short axis of the molecules. The kMC trajectories support the charge transport network picture reported previously, namely:

- 1D for longer alkyl chains as *hex,tbu-* and *oct,tbu-D2A1*;
- 2D hole transport for molecules having short lateral alkyl chains, such as *me,tbu-* and *bpr,tbu-D2A1*;
- 3D for medium size lateral alkyl chains, like *nbu,tbu-* and *nbu,nbu-D2A1*.

Such classification defines the charge transport topologies as 1D, when the spatial displacement of the charge is larger by at least a factor of 2 for one direction over the two other directions. As 2D, when the spatial displacement is about the same in two directions, and at least a factor of 2 smaller in the third direction. Consequently, a 3D topology is defined as approximately similar displacements in all directions (see computed direction dependent mobilities in the ESI,† Table S13). The computed Brownian hole mobility, in the absence of disorder, is the highest for *me,tbu-* ($0.206 \text{ cm}^2 \text{ V}^{-1} \text{ s}^{-1}$, 2D transport network) and *bpr,tbu-* ($0.161 \text{ cm}^2 \text{ V}^{-1} \text{ s}^{-1}$, 2D transport), and it decreases up to a factor of 4 for *hex,tbu-* and *oct,tbu-* (0.067 and $0.065 \text{ cm}^2 \text{ V}^{-1} \text{ s}^{-1}$, respectively, both 1D transport), and up to an order of magnitude for *nbu,tbu-* and *nbu,nbu-* (0.020 and $0.030 \text{ cm}^2 \text{ V}^{-1} \text{ s}^{-1}$, both 3D transport), see values in Table 2.

For *me,tbu-D2A1*, inter-columnar transfer rates are two orders of magnitude smaller than intra-columnar hops, leading to a sequence of fast ($1.5 \times 10^{13} \text{ s}^{-1}$), short-range (6.164 Å) hops along the column and slow ($8.9 \times 10^{11} \text{ s}^{-1}$), long-range (10.746 Å) hops between columns, resulting in 2D hole transport within the yz plane (Fig. 3a and ESI,† Fig. S2, Table S3).

The *bpr,tbu-D2A1* has an intra-columnar asymmetry in the transfer rates (A and A', Table 1), which could lead to charge trapping or delay phenomena. Inter-columnar transfer rates are one order of magnitude smaller than the highest intra-columnar hops, leading to an alternating sequence of fast ($4.4 \times 10^{13} \text{ s}^{-1}$), short-range (6.447 Å) hops within the column

and slow ($1.0 \times 10^{12} \text{ s}^{-1}$), long-range (12.635 Å) hops between columns, showing a 2D transport path (Fig. 3b, and ESI,† Fig. S3 and Table S4). For *nbu,tbu-* and *nbu,nbu-D2A1*, the difference between intra- and inter-columnar transfer rates almost vanishes, leading to isotropic 3D transport pathways (Fig. 3c and d, also ESI,† Fig. S4 and S5, Tables S5 and S6). Finally, for merocyanines characterized by 1D transport (*hex,tbu-* and *oct,tbu-D2A1*), intra-columnar and inter-columnar transfer rates differ by three orders of magnitude (Table 1). For such reasons, hops occur almost exclusively along the direction of the higher transfer rates (intra-column), corresponding to the x axis (Fig. 3e and f, also ESI,† Fig. S6 and S7, Tables S7 and S8). Couplings along the column are asymmetric, resulting in asymmetric transfer rates differing by a factor of 2 for *hex,tbu-D2A1*, and by an order of magnitude for *oct,tbu-D2A1* (Table 1). Such asymmetries can limit the final hole mobility, resulting in charge trapping for several hops within a dimer.

The computed hole mobilities of R_1, R_2^- -**D2A1**, in the absence of static and dynamic disorder effects, range from 2×10^{-1} to $2 \times 10^{-2} \text{ cm}^2 \text{ V}^{-1} \text{ s}^{-1}$ (Table 2), with *me,tbu-* and *bpr,tbu-D2A1* showing the highest values. Experimental charge mobilities, as taken from the literature, are measured on polycrystalline OFETs, showing high values for *bpr,tbu-* and *nbu,tbu-D2A1* (0.18 and $0.14 \text{ cm}^2 \text{ V}^{-1} \text{ s}^{-1}$), followed by *hex,tbu-D2A1* ($0.050 \text{ cm}^2 \text{ V}^{-1} \text{ s}^{-1}$), *nbu,nbu-D2A1* ($0.026 \text{ cm}^2 \text{ V}^{-1} \text{ s}^{-1}$) and *me,tbu-D2A1* ($0.018 \text{ cm}^2 \text{ V}^{-1} \text{ s}^{-1}$).⁴ Despite being of the same order of magnitude, these data differ from the computed values. Reasons for such discrepancy are multiple, and they can be related to various factors, which can be traced back to both experimental (*e.g.*, grain boundaries, impurities, and the size and orientation of the crystal domains) and theoretical (*e.g.*, the absence of static and dynamic disorder effects, the validity of the hopping-regime, the absence of grain boundaries and semi-crystalline regions) aspects.

Table 2 compares the results discussed above with a prototypical merocyanine belonging to the **D1A1** class, namely *pyrl,tbu-D1A1* (see the chemical structure in Fig. 1a), and already studied by us.⁹ Such species, despite featuring a



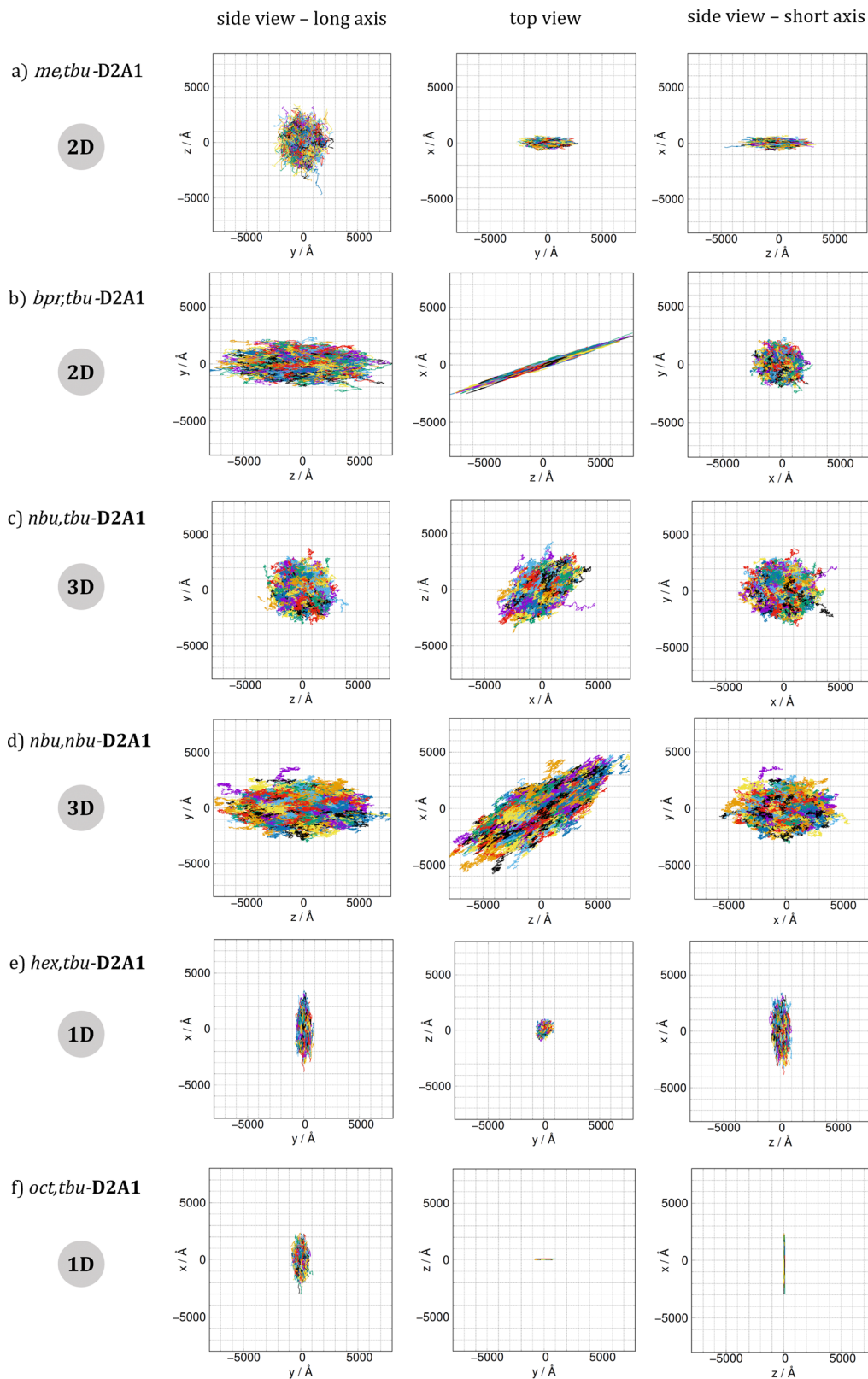


Fig. 3 kMC trajectories (1000, 10^5 steps each) for each crystal of **D2A1** (a) *me,tbu*-, (b) *bpr,tbu*-, (c) *nbu,tbu*-, (d) *nbu,nbu*-, and (e) *hex,tbu*-, (f) *oct,tbu*-**D2A1** in the absence of disorder. kMC trajectories are reported for the three Cartesian planes xy , xz and yz . The planes were ordered as: the side view (first column) onto the long molecular axis, the top (second column) and the side view (third column) onto the short molecular axis.



Table 2 Average computed charge mobilities ($\text{cm}^2 \text{V}^{-1} \text{s}^{-1}$) μ evaluated by assuming a Brownian diffusion mechanism via the Einstein–Smoluchowski equation without (μ_{wo}) and with the presence of static energetic disorder (μ_{s}). ΔE_{ij} (eV) is the computed maximum of the site energy differences together with the mobility ratio $\frac{\mu_{\text{wo}}}{\mu_{\text{s}}}$. The charge transport topology is reported in parenthesis for each case

R_1, R_2 - D2A1	μ_{wo} ($\text{cm}^2 \text{V}^{-1} \text{s}^{-1}$) without disorder	ΔE_{ij} (eV)	μ_{s} ($\text{cm}^2 \text{V}^{-1} \text{s}^{-1}$) static disorder	$\frac{\mu_{\text{wo}}}{\mu_{\text{s}}}$
<i>me,tbu-</i>	0.206 (2D)	± 0.125	0.105 (2D)	2
<i>bpr,tbu-</i>	0.161 (2D)	± 0.358	0.007 (1D)	23
<i>nbu,tbu-</i>	0.020 (3D)	± 0.683	0.002 (1D/2D)	10
<i>nbu,nbu-</i>	0.030 (3D)	± 0.451	0.004 (1D/2D)	8
<i>hex,tbu-</i>	0.067 (1D)	± 0.124	0.018 (1D/2D)	4
<i>oct,tbu-</i>	0.065 (1D)	± 0.124	0.017 (1D)	4
<i>pyrl,tbu-D1A1</i>	0.160 (1D)	± 0.233	0.042 (1D)	4

different donor unit (**D1**) and a 1D columnar packing in the solid state (see Fig. S8, ESI[†]), shows a computed Brownian hole mobility of $0.160 \text{ cm}^2 \text{V}^{-1} \text{s}^{-1}$ (semi-classical Marcus rates) that is of the same order of magnitude of both 1D and 2D charge transport cases predicted for the **D2A1** species. As discussed in the next sections, the comparison between merocyanines belonging to these two classes (**D1A1** vs. **D2A1**) allows to draw more general structure–property relationships and to get insights into the role played by static and energetic disorder effects (see below) on this family of organic conjugated molecules.

Static (energetic) disorder

Electrostatic and polarization effects^{51,65–68} impact the site energy differences ΔE_{ij} , thereby influencing the transfer rates (see eqn (1)), the charge mobility, and the topology of the charge transport network.^{69,70} While one-dimensional charge transport is prone to structural defects, the prior effect of static disorder is to interconnect or disconnect certain pathways, thus determining a new topological connectivity.⁷¹ Such effects have never been modelled nor discussed in the literature of merocyanines, and we expect a strong impact of the polarization effects onto the charge transport properties of polar molecules in condensed phases.⁷²

The R_1, R_2 -**D2A1** library is an ideal platform to explore the impact of the energetic disorder over various charge transport networks, ranging from 1D, 2D up to 3D. Furthermore, the evaluation of ΔE_{ij} for *pyr,tbu-D1A1* allows the comparison between different **D–A** classes, together with the definition of general design guidelines about merocyanines.

The computed ranges (*i.e.*, min/max values) of the site energy differences (ΔE_{ij}) are reported in Table 2, while their standard deviation and distributions are included in the ESI,[†] Fig. S10 and Table S10. The smallest ΔE_{ij} are calculated for *hex,tbu-*, *me,tbu-* and *oct,tbu-D2A1* (± 0.125 eV), whereas it is largest for *nbu,tbu-D2A1* (± 0.683 eV). For comparison, for *pyrl,tbu-D1A1*, ΔE_{ij} is ± 0.233 eV, being below *bpr,tbu-* (± 0.358 eV) and *nbu,nbu-D2A1* (± 0.451 eV).

The ΔE_{ij} (± 0.124 – 0.683 eV) are of the same order of magnitude or higher than the total (*i.e.*, inner + outer sphere) reorganization energy of merocyanines (min. $\lambda = 0.177$ eV for *pyrl,tbu-D1A1*, max. $\lambda = 0.229$ eV for *bpr,tbu-D2A1*). Consequently, they will affect the final Marcus transfer rate constants

via the $(\Delta E_{ij} + \lambda)^2$ term (eqn (1)). By definition, ΔE_{ij} are site-dependent properties. Therefore, certain directions within the crystal will be more affected than others by the inclusion of polarization effects.

By re-computing the Brownian kMC hole mobility in the presence of static disorder (μ_{s}), we observe a drop of μ (from a factor of two to more than an order of magnitude) for each R_1, R_2 -**D2A1** crystal (Table 2). The lowering of the charge mobility by turning on the polarizable effects is expected and it is in line with previous literature data on other organic semiconductors.^{15,72}

Some interesting trends can be observed. For *me,tbu-*, *hex,tbu-* and *oct,tbu-D2A1*, which are characterised by high electronic couplings ($J_{ij} > 50$ meV) and site energy differences ($|\Delta E_{ij}| = 0.124$ – 0.125 eV) smaller than the total reorganization energy (0.217 – 0.227 eV), the charge transport pathways are almost not influenced by the presence of the energetic disorder, preserving the charge transport dimensionality as in the absence of static disorder. The reason for this behaviour is two-fold: (i) the site energy difference distribution is very narrow around zero, and (ii) the $(\Delta E_{ij} + \lambda)^2$ term in the semi-classical Marcus equation (eqn (1)) can be small or vanishing, thus leading to rate constants that are prevalently ruled by the electronic couplings.

Instead, *bpr,tbu-*, *nbu,tbu-* and *nbu,nbu-D2A1* feature medium to small electronic couplings ($J_{ij} < 40$ meV) and site energy differences ($|\Delta E_{ij}| = 0.358$ – 0.683 eV) larger than the total reorganization energy (0.217 – 0.229 eV); therefore, the charge transport network changes notably by varying its topology. This is because the distribution of ΔE_{ij} is broader than the previous cases, and the $(\Delta E_{ij} + \lambda)^2$ term can be either small or large; therefore, the Marcus regime is highly affected, as well as the rate constants.

Notably, energetic disorder impacts the charge transport topology too. In detail, *me,tbu-D2A1* has high intra-columnar couplings (56 meV) and medium/small inter-columnar electronic integrals (16 meV). Both pathways are preserved in the presence of static disorder, maintaining overall a 2D charge transport (ESI,[†] Fig. S11). Also, for *hex,tbu-* and *oct,tbu-D2A1*, characterized by high intra- and low inter-columnar couplings, the charge transport network is preserved as in the absence of static disorder (see transfer rates in the ESI,[†] Table S10 and Fig. S15 and S16). For the case of *bpr,tbu-D2A1* instead, characterized by medium/small intra- and inter-columnar couplings



and high ΔE_{ij} , the intra-column hops are strongly affected decreasing the transfer rates by orders of magnitude (see transfer rates in the ESI,[†] Tables S4, S10 and Fig. S12), therefore changing the charge transport network from 2D to a quasi 1D. Similarly, for *nbu,tbu-* and *nbu,nbu-D2A1*, characterized by medium/small couplings and high ΔE_{ij} , the charge transport network remarkably changes by localizing the hopping trajectories in few dimensions (ESI,[†] Table S10 and Fig. S13 and S14).

Considering the **D1A1** class, namely *pyrl,tbu-D1A1*, the high intra-columnar couplings, together with the narrow site energy difference distribution and a ΔE_{ij} comparable with λ , lead to minor changes in the charge transport network (ESI,[†] Fig. S17) with respect to the absence of static disorder, paralleling the cases of *me,tbu-*, *hex,tbu-* and *oct,tbu-D2A1*.

Overall, in the presence of static disorder, large site energy distributions ($\max(|\Delta E_{ij}|) \gg \lambda$) affect the transport network the most, for the case of *bpr,tbu-*, *nbu,tbu-* and *nbu,nbu-D2A1* characterized by the highest decreases in μ (from a factor of 8 up to 23, see Table 2). For small site energy distributions ($\max(|\Delta E_{ij}|) \leq \lambda$) and large couplings, for *me,tbu-*, *hex,tbu-* and *oct,tbu-D2A1*, the charge transport networks are preserved and the mobility value reduces by a factor of 2 up to 4 (Table 2).

Dynamic (thermal) disorder

Dynamic disorder effects, *i.e.* the variations of the coupling integrals as induced by thermal oscillations, including both intra- and inter-molecular vibrations (*e.g.*, the centre of mass translations, librations and rotations), were computed through

the evaluation of the Fourier Transform (FT) of the time-dependent auto-correlation function (ACF) of the coupling integrals $\langle J(t + \tau)J(t) \rangle / \langle J(t)^2 \rangle$ (see details in ref. 59, 73 and 74 and ESI,[†] Fig. S17 and S18). Couplings were computed by sampling the trajectories extracted from the MD simulations of three crystal structures, namely *pyrl,tbu-D1A1*, *me,tbu-D2A1* and *nbu,tbu-D2A1*. The three cases are considered as representative case studies for merocyanines featuring different **D-A** moieties and hole charge transport network topologies, respectively, 1D, 2D and 3D. The 1D and 2D cases (*pyrl,tbu-D1A1* and *me,tbu-D2A1*) show strong anisotropy in the coupling network, featuring high intra-columnar transfer integrals ($J_{ij} > 50$ meV) and low ($J_{ij} < 4$ meV, 1D case) or medium ($J_{ij} = 16$ meV, 2D case) electronic interactions across columns. The 3D case (*nbu,tbu-D2A1*) shows low transfer integrals ($J \leq 16$ meV) in all directions.

Fig. 4 reports the distribution and the time-dependent fluctuations for the highest J_{ij} (ESI,[†] Fig. S20 for the coupling distributions of other dimers). For all merocyanines, broad distributions and large fluctuations of J_{ij} are computed. The distribution of the transfer integrals (J) can be well fitted by a Gaussian function. The average value ($\langle J \rangle$) increases for all merocyanines, as compared to the respective static (frozen crystal) value (Fig. 4 and ESI,[†] Table S11). Such an increase can be inferred to (intrinsic) thermal effects as well as to the quality (*e.g.*, parameterization of bonded and non-bonded terms) of the force-field, impacting the relative positions and distributions of the molecules during the MD simulations.

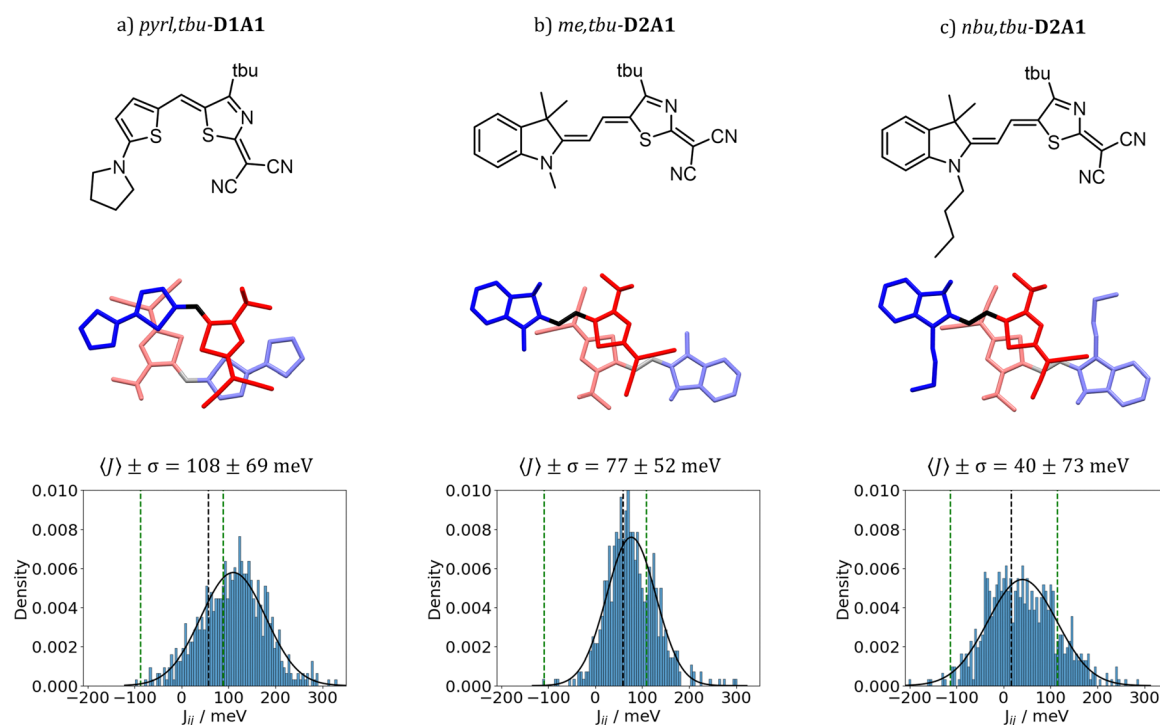


Fig. 4 Dynamic disorder effects on dimer A of (a) *pyrl,tbu-D1A1*, (b) *me,tbu-* and (c) *nbu,tbu-D2A1* (chemical structures and dimer geometries on top), showing the distribution of the coupling integrals J_{ij} (Gaussian fit, black line) calculated at the ZINDO/S level, bottom panels. The mean value ($\langle J \rangle$) and standard deviation σ are reported as well. Black dashed lines represent the value of the electronic coupling for the case of frozen crystals at the ZINDO/S level (*i.e.*, XRD experimental structure), and the green lines mark the $\pm\lambda/2$ energy range, remarking the validity of the non-adiabatic regime.²¹



The thermal broadening of the transfer integrals, namely the standard deviation σ , is 52 meV for *me,tbu-D2A1*, 73 meV for *nbu,tbu-D2A1* and 69 meV for *pyrl,tbu-D1A1* (Fig. 4 and ESI,† Table S11). From the analysis of the FT of the coupling ACF (ESI,† Fig. S18), we observed that the active oscillations affecting the electronic couplings the most are those below 100 cm⁻¹. Such frequencies, as documented in the literature for other conjugated compounds, can be associated with inter-molecular normal modes (*e.g.*, translation, libration) involving the molecular backbone and the lateral chains of the molecules.^{12,19,20,27,75–77}

The spread of the coupling integrals, as induced by thermal disorder, leads to the question, whether the non-adiabatic hopping mechanism is the suitable model to describe hole transport in merocyanines. In the absence of thermal oscillations (frozen crystal), the parameter $\xi = 2|J|/\lambda$ ranges from 0.1 for *nbu,tbu-D2A1* up to 0.6 for *pyrl,tbu-D1A1* (ESI,† Table S11). Such values lie within the range of the hopping regime (*i.e.*, validity of the non-adiabatic semi-classical Marcus approach),^{11,21,32,78} with only *pyrl,tbu-D1A1* being relatively close to an intermediate regime. Inclusion of averaged coupling ($\langle J \rangle$) in the evaluation of ξ ($\xi = 2|\langle J \rangle|/\lambda$)⁷⁹ leads to values of 0.4 for *nbu,tbu-D2A1*, 0.7 for *me,tbu-D2A1* and up to 1.2 for *pyrl,tbu-D1A1*. This increase might suggest that different charge transport regimes than hopping should be considered. An in-depth investigation of such effects, together with the inclusion of charge transport schemes which go beyond the non-adiabatic Marcus approach,⁸⁰ is currently under investigation in our group and they will be the subject for future works.

Albeit keeping a non-adiabatic regime (thermalized limit), we checked the impact of considering a second order (thermal) correction to the calculation of the non-adiabatic transfer

rates, as suggested by Ratner and Troisi.^{73,79} The second order correction (ESI,† Section S10) to the non-adiabatic transfer rate is proportional to the factor $\left(1 - \frac{\langle J \rangle^2}{\langle J^2 \rangle}\right)$. When $\frac{\langle J \rangle^2}{\langle J^2 \rangle}$ is close to unity, the impact of thermal oscillations is weak, and the thermal corrections to the transfer rates are negligible. In such cases, the use of eqn (1), by replacing the static J with the average of the coupling square $\langle J^2 \rangle$, is acceptable.⁷⁹ However, when $\frac{\langle J \rangle^2}{\langle J^2 \rangle}$ is smaller than unity, the thermal corrections become relevant.²⁴ As also reported by Martinelli *et al.*,²⁴ an equivalent description is given by introducing the parameter η , defined as $\eta = \frac{\langle J_{ij} \rangle}{\sigma}$, with $\sigma = \sqrt{\langle J^2 \rangle - \langle J \rangle^2}$. Values of $\eta \geq 0.5$ suggest the impact of lattice vibrations to be weak on the transfer rate equation, whereas values < 0.5 imply a global increase of the transfer rates. For *me,tbu-D2A1* and *pyrl,tbu-D1A1*, with $\eta = 1.5$ and 1.6, respectively, significantly larger than 0.5, consequently the non-adiabatic transfer rates are weakly affected by thermal corrections (see also $\frac{\langle J \rangle^2}{\langle J^2 \rangle}$ values in the ESI,† Table S11). For *nbu,tbu-D2A1*, with $\eta = 0.5$ and $\frac{\langle J \rangle^2}{\langle J^2 \rangle} = 0.2$, thermal corrections can enhance significantly the non-adiabatic transfer rates.

Given the above assumptions, in the frame of the non-adiabatic regime,⁷⁹ we have re-computed the transfer rate constants and kMC mobilities by considering the thermalized value of the coupling integrals ($\langle J^2 \rangle$) in the rate equation (eqn (1)), without taking into account the effect of static disorder (ESI,† Table S12). Thermalized Brownian hole mobilities (μ_t) overall increase, raising for *me,tbu-D2A1* by a factor of

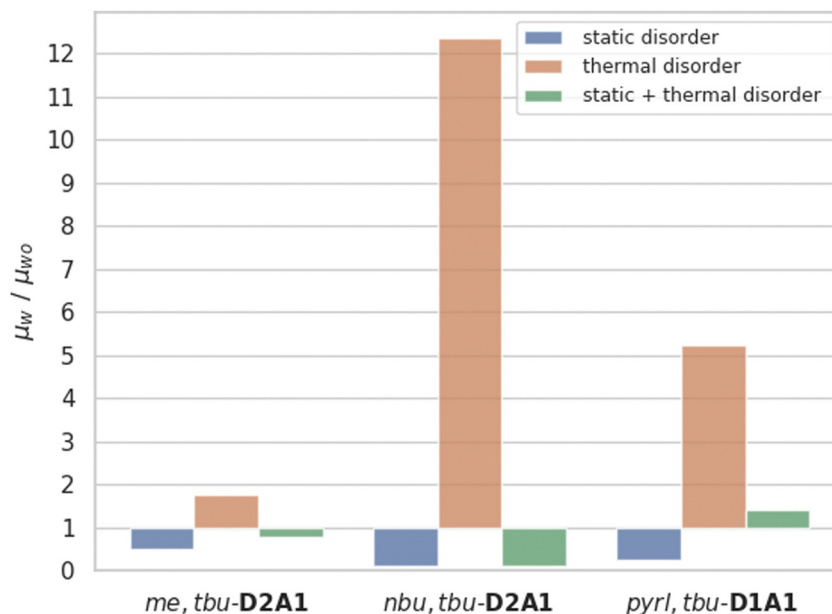


Fig. 5 Ratio of the computed hole mobilities (μ_w/μ_{w0}) with the static (blue), thermal (red) and both static and thermal disorder effects (green) to the Brownian charge mobility without disorder effects for *me,tbu-*, *nbu,tbu-D2A1* and *pyrl,tbu-D1A1*.



2, for *nbu,tbu-D2A1* by a factor of 12 and for *pyrl,tbu-D1A1* by a factor of 5 (Fig. 5 and ESI,† Table S12). The increase in charge mobility is remarkable for both *nbu,tbu-D2A1* and *pyrl,tbu-D1A1*. For the first species, medium/small electronic couplings (J) and high thermal oscillations (J^2) favour the opening of effective hole transfer channels, thus increasing the mobility. The computed thermal averaged charge mobility ($0.247 \text{ cm}^2 \text{ V}^{-1} \text{ s}^{-1}$) is of the same order of magnitude to the average experimental device mobility ($0.87 \text{ cm}^2 \text{ V}^{-1} \text{ s}^{-1}$), as measured on single crystal OFETs.⁸ For *pyrl,tbu-D1A1*, the largest increase in the charge mobility is mainly due of the increment of the electronic coupling values for the only-effective charge transport channel that is the intra-columnar one.

Static and dynamic disorder effects

Lastly, we combined both static and dynamic disorder effects, thus evaluating the charge mobility by including the averaged square couplings (J^2) as well as the site energy differences (the latter computed on the crystal structure) μ_{s+t} . When both effects are considered, the Brownian hole mobilities generally increase as compared to pure static disorder (except of *nbu,tbu-D2A1*, see below) and decrease as compared to the pure thermal disorder (ESI,† Table S12). The detrimental effects of static disorder are partially compensated by thermal motions. Such trends are summarized in Fig. 5, showing the ratio between the computed Brownian hole mobility in the presence of different kinds of disorder ((a) static – blue bars, (b) thermal – orange, and (c)

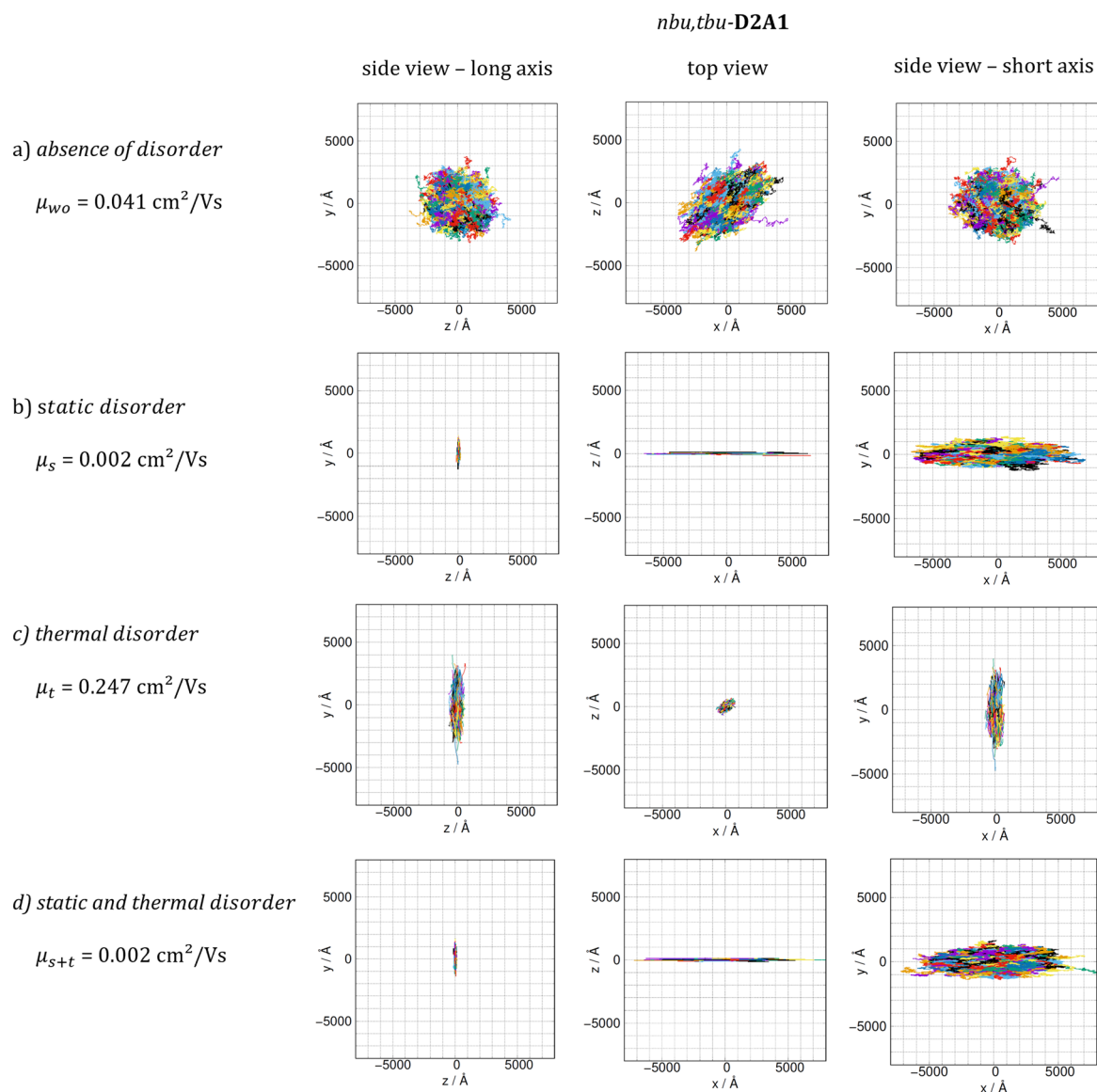


Fig. 6 Computed hole mobility μ and plot of 1000 kMC trajectories (each consisting of 10^5 steps) for *nbu,tbu-D2A1*, (a) without disorder effects, (b) with static disorder effects, (c) with thermal disorder effects and (d) with both static and thermal disorder effects included. Trajectories are reported for the three Cartesian planes, namely xy , xz and yz . For clarity, the three Cartesian planes were ordered in such a way to correspond to the side view onto the molecules long axis, the top view and the side view onto the molecule's short axis.



static and thermal – green) with respect to those computed without any disorder. For *nbu,tbu-* and *me,tbu-D2A1*, the charge mobility computed in the presence of both types of disorder is dominated by the static one, which globally limits the charge diffusion. For *pyrl,tbu-D1A1* instead, the static disorder is compensated by the thermal fluctuations and the final hole mobility in the presence of both disorder effects is larger than that without any disorder.

For *nbu,tbu-D2A1*, in Fig. 6, the kMC hole trajectories are reported for all cases previously considered: (a) non-adiabatic transfer rates without disorder effects, (b) with static disorder effects, (c) with dynamic disorder effects, and (d) with both static and dynamic disorder effects. Without any disorder effects, the *nbu,tbu-D2A1* charge transport pathways form an isotropic 3D transport network (Fig. 6a). In the presence of static disorder, the network is reduced to an anisotropic quasi-1D topology, leading to an overall decrease in mobility (Fig. 6b). With dynamic disorder, the charge transport is enhanced, and the transport topology is highly anisotropic along the columns (Fig. 6c). The inclusion of both, static and dynamic disorder, affords a similar quasi-1D topology (Fig. 6d) as in the presence of just the static effects (Fig. 6b), and the charge mobility is reduced by a factor of 10 compared to the case without any disorder effects (Table S12, ESI†). In ESI,† (Fig. S11 and S17) the results are reported for *me,tbu-D2A1* and *pyrl-D1A1*, where the presence of static and dynamic disorder effects affects the computed charge mobility, however maintaining the charge transport topology (2D and 1D, respectively) as in the absence of disorder.

Generally, our data can parallel those already reported by Vehoff *et al.*⁷¹ for other organic single crystals constituted by apolar molecules (*e.g.*, rubrene), that is the presence of (structural) disorder can reduce or increase the charge carrier mobility, depending also on the dimensionality of the charge transfer network. The one-dimensional transport is prone to structural defects, instead shifted anti-parallel alignments allow for 2D or 3D dimensional charge transport, reducing the influence of structural defects.

Conclusions

Merocyanines are D–A conjugated molecules considered as prototypical building blocks for studying the structure–property relationships of highly polar organic semiconductors. Tuning their D–A moieties and engineering their side groups are effective strategies to influence their supramolecular order in the solid state and their charge/exciton transport properties. Recently, experimental evidence reported the possibility for merocyanine single crystals to reach as high hole mobility (up to $2 \text{ cm}^2 \text{ V}^{-1} \text{ s}^{-1}$) as state-of-the-art small molecules (*e.g.*, acenes and thioacenes). However, very few atomistic investigations aiming at modelling their charge transport properties are present in the literature, resulting in a general lack of fundamental understanding. We fill the gap, reporting here an in-depth computational investigation over a library of

merocyanines, showing how static and dynamic disorder effects influence the charge transport parameters and mobility, by impacting both the transfer rates and the topology of the charge transport networks in single crystals. We considered seven merocyanines differing by their donor unit and side chains, showing different packing motifs in the solid state. All merocyanines pack in an antiparallel slipped fashion along the $\pi\pi$ -direction. Depending on the side groups, crystals form quasi 1D stacks that by interacting with neighbouring columns create interconnected 2D layers (mostly due to extended and flexible side chains). As the reorganization energies are similar for all species, the charge transfer rates and mobilities depend mainly on the coupling integrals and site energy differences.

Our simulations show that for merocyanines characterized by high intra-column charge transfer integrals ($> 50 \text{ meV}$) and low inter-column couplings ($< 10 \text{ meV}$), a clear 1D transport network appears. For medium to small intra-columnar transfer integrals (10–40 meV), interactions across columns become relevant, leading to 2D or 3D transport. The computed mobilities are the highest for the 2D cases and the lowest for the 3D cases, reflecting the values of the coupling integrals.

When static disorder effects are included, a decrease in the charge mobility is computed for all species. Our simulations reveal that for those merocyanines characterized by small electronic couplings ($< 40 \text{ meV}$), when the site energy differences are larger than or similar to the reorganization energy, the charge transport network is affected the most, changing from 3D (without disorder) to 1D (with disorder), as the case of *nbu,tbu-D2A1*. Conversely, for those species featuring large charge transfer integrals ($> 50 \text{ meV}$) and site energy differences similar to the reorganization energy, the transport network is preserved, for *pyrl,tbu-D1A1* and *me,tbu-D2A1*.

Dynamic disorder leads on average to an enhancement of the charge transport along these directions where the electronic couplings are the highest. The non-adiabatic hypothesis holds for most of the merocyanines investigated here, with only one case (*pyrl,tbu-D1A1*) being relatively close to an intermediate (*i.e.*, small-polaron hopping) charge transport regime. Thermalized Brownian hole mobilities increase, raising up to a factor of 12 with respect to the absence of thermal effects. The increase in charge mobility is remarkable for both *nbu,tbu-D2A1* and *pyrl,tbu-D1A1*.

When both static and dynamic disorder effects are considered, our simulations reveal that the former affects the charge mobility the most. We conclude that polarization effects are detrimental for the charge transport of polar dyes, and such a decrease cannot be compensated by thermal effects, even though the latter, for the case of merocyanines, leads to a general enhancement of the transfer rates.

Given the current investigation, and considering our previous computational study⁹ as well as the broad set of experimental data available in the literature,⁴ the best strategy to design merocyanines whose charge mobility is most resilient to static and dynamic disorder effects, can be to include strong donor–acceptor units, connected by a short, conjugated bridge (*e.g.*, methylene, ethylene) and small lateral groups (*e.g.*, methyl



and *n*-butyl). These features would lead to polar dyes, characterised by low reorganisation energy and solid state anti-parallel brick-wall-like packing, which minimizes polarization effects and maximizes the enhancement of the charge mobility due to thermal oscillations.

Data availability

The data supporting this article have been included as part of the ESI.†

Conflicts of interest

There are no conflicts to declare.

Acknowledgements

K. M., D. F., N. G., S. G. and R. H. acknowledge the DFG Research Training Group 2591 “Template-designed Organic Electronics (TIDE)” for supporting their research. They also acknowledge the Regional Computing Centre (RRZK) of the University of Cologne for providing computing time and resources on the HPC RRZK CHEOPS. D. F. and F. N. acknowledge the RFO funds from the University of Bologna. F. N. acknowledges the European Union—Next Generation EU under the Italian National Recovery and Resilience Plan (PNRR M4C2, Investment 1.4—Call for tender no. 3138 dated 16/12/2021—CN00000013 National Centre for HPC, Big Data and Quantum Computing (HPC)—CUP J33C22001170001). D. F. acknowledges the Global Faculty Program of the University of Cologne within the focus area “Quantum Matter and Materials (QM2)”, the National Recovery and Resilience Plan (NRRP), Mission 04 Component 2 Investment 1.5 – NextGenerationEU, Call for tender no. 3277 dated 30/12/2021, Award Number: 0001052 dated 23/06/2022, and the National Project funded by the European Union – Next Generation EU, Project title “Modelling and design of organic conjugated redox materials for energy-saving applications: a bottom-up strategy”, code MUR 2022WKTH9E – CUP J53D23008810006.

References

- 1 F. Würthner, R. Wortmann, R. Matschiner, K. Lukaszuk, K. Meerholz, Y. DeNardin, R. Bittner, C. Bräuchle and R. Sens, *Angew. Chem., Int. Ed. Engl.*, 1997, **36**, 2765–2768.
- 2 F. Würthner, R. Wortmann and K. Meerholz, *ChemPhysChem*, 2002, **3**, 17–31.
- 3 F. Würthner and K. Meerholz, *Chem. – Eur. J.*, 2010, **16**, 9366–9373.
- 4 A. Liess, L. Huang, A. Arjona-Esteban, A. Lv, M. Gsänger, V. Stepanenko, M. Stolte and F. Würthner, *Adv. Funct. Mater.*, 2015, **25**, 44–57.
- 5 T. Kim, S. Kang, E. Kirchner, D. Bialas, W. Kim, F. Würthner and D. Kim, *Chem*, 2021, **7**, 715–725.
- 6 A. Liess, A. Arjona-Esteban, A. Kudzus, J. Albert, A.-M. Krause, A. Lv, M. Stolte, K. Meerholz and F. Würthner, *Adv. Funct. Mater.*, 2019, **29**, 1805058.
- 7 H. Bürckstümmer, N. M. Kronenberg, M. Gsänger, M. Stolte, K. Meerholz and F. Würthner, *J. Mater. Chem.*, 2010, **20**, 240–243.
- 8 A. Liess, M. Stolte, T. He and F. Würthner, *Mater. Horiz.*, 2016, **3**, 72–77.
- 9 N. Gildemeister, G. Ricci, L. Böhner, J. M. Neudörfl, D. Hertel, F. Würthner, F. Negri, K. Meerholz and D. Fazzi, *J. Mater. Chem. C*, 2021, **9**, 10851–10864.
- 10 A. Landi and A. Troisi, *J. Phys. Chem. C*, 2018, **122**, 18336–18345.
- 11 A. Troisi, *Chem. Soc. Rev.*, 2011, **40**, 2347–2358.
- 12 S. Di Motta, M. Siracusa and F. Negri, *J. Phys. Chem. C*, 2011, **115**, 20754–20764.
- 13 C. Poelking, E. Cho, A. Malafeev, V. Ivanov, K. Kremer, C. Risko, J.-L. Brédas and D. Andrienko, *J. Phys. Chem. C*, 2013, **117**, 1633–1640.
- 14 J. Cornil, S. Verlaak, N. Martinelli, A. Mityashin, Y. Olivier, T. van Regemorter, G. D’Avino, L. Muccioli, C. Zannoni, F. Castet, D. Beljonne and P. Heremans, *Acc. Chem. Res.*, 2013, **46**, 434–443.
- 15 M. Schrader, C. Körner, C. Elschner and D. Andrienko, *J. Mater. Chem.*, 2012, **22**, 22258.
- 16 V. Coropceanu, J. Cornil, D. A. Da Silva Filho, Y. Olivier, R. Silbey and J.-L. Brédas, *Chem. Rev.*, 2007, **107**, 926–952.
- 17 S. Fratini, D. Mayou and S. Ciuchi, *Adv. Funct. Mater.*, 2016, **26**, 2292–2315.
- 18 T. F. Harrelson, V. Dantanarayana, X. Xie, C. Koshnick, D. Nai, R. Fair, S. A. Nuñez, A. K. Thomas, T. L. Murrey, M. A. Hickner, J. K. Grey, J. E. Anthony, E. D. Gomez, A. Troisi, R. Faller and A. J. Moulé, *Mater. Horiz.*, 2019, **6**, 182–191.
- 19 E. Di Donato, R. P. Fornari, S. Di Motta, Y. Li, Z. Wang and F. Negri, *J. Phys. Chem. B*, 2010, **114**, 5327–5334.
- 20 S. Canola and F. Negri, *Phys. Chem. Chem. Phys.*, 2014, **16**, 21550–21558.
- 21 H. Oberhofer, K. Reuter and J. Blumberger, *Chem. Rev.*, 2017, **117**, 10319–10357.
- 22 J. Blumberger, *Chem. Rev.*, 2015, **115**, 11191–11238.
- 23 S. Giannini, O. G. Zogios, A. Carof, M. Ellis and J. Blumberger, *Adv. Theory Simul.*, 2020, **3**, 2000093.
- 24 N. G. Martinelli, Y. Olivier, S. Athanasopoulos, M.-C. Ruiz Delgado, K. R. Pigg, D. A. Da Silva Filho, R. S. Sánchez-Carrera, E. Venuti, R. G. Della Valle, J.-L. Brédas, D. Beljonne and J. Cornil, *ChemPhysChem*, 2009, **10**, 2265–2273.
- 25 V. Coropceanu, R. S. Sánchez-Carrera, P. Paramonov, G. M. Day and J.-L. Brédas, *J. Phys. Chem. C*, 2009, **113**, 4679–4686.
- 26 R. S. Sánchez-Carrera, P. Paramonov, G. M. Day, V. Coropceanu and J.-L. Brédas, *J. Am. Chem. Soc.*, 2010, **132**, 14437–14446.
- 27 A. Troisi and G. Orlandi, *J. Phys. Chem. A*, 2006, **110**, 4065–4070.
- 28 A. S. Eggeman, S. Illig, A. Troisi, H. Sirringhaus and P. A. Midgley, *Nat. Mater.*, 2013, **12**, 1045–1049.



- 29 T. Nemataram and A. Troisi, *Mater. Horiz.*, 2020, **7**, 2922–2928.
- 30 A. Giraldo, L. Grisanti, M. Masino, A. Brillante, R. G. Della Valle and E. Venuti, *J. Chem. Phys.*, 2011, **135**, 84701.
- 31 H. Yang, F. Gajdos and J. Blumberger, *J. Phys. Chem. C*, 2017, **121**, 7689–7696.
- 32 S. Giannini, A. Carof, M. Ellis, H. Yang, O. G. Zigos, S. Ghosh and J. Blumberger, *Nat. Commun.*, 2019, **10**, 3843.
- 33 M. A. Dettmann, L. S. R. Cavalcante, C. Magdaleno, K. Masalkovaitė, D. Vong, J. T. Dull, B. P. Rand, L. L. Daemen, N. Goldman, R. Faller and A. J. Moulé, *J. Chem. Theory Comput.*, 2021, **17**, 7313–7320.
- 34 D. Vong, T. Nemataram, M. A. Dettmann, T. L. Murrey, L. S. R. Cavalcante, S. M. Gurses, D. Radhakrishnan, L. L. Daemen, J. E. Anthony, K. J. Koski, C. X. Kronawitter, A. Troisi and A. J. Moulé, *J. Phys. Chem. Lett.*, 2022, **13**, 5530–5537.
- 35 A. Ojala, H. Bürckstümmer, J. Hwang, K. Graf, B. von Vacano, K. Meerholz, P. Erk and F. Würthner, *J. Mater. Chem.*, 2012, **22**, 4473–4482.
- 36 T. L. Murrey, D. Hertel, J. Nowak, R. Bruker, T. Limböck, J. Neudörfl, S. Rüh, J. Schelter, S. Olthof, A. Radulescu, A. J. Moulé and K. Meerholz, *J. Phys. Chem. C*, 2020, **124**, 19457–19466.
- 37 M. J. Frisch, G. W. Trucks, H. B. Schlegel, G. E. Scuseria, M. A. Robb, J. R. Cheeseman, G. Scalmani, V. Barone, G. A. Petersson, H. Nakatsuji, X. Li, M. Caricato, A. V. Marenich, J. Bloino, B. G. Janesko, R. Gomperts, B. Mennucci, H. P. Hratchian, J. V. Ortiz, A. F. Izmaylov, J. L. Sonnenberg, D. Williams-Young, F. Ding, F. Lipparini, F. Egidi, J. Goings, B. Peng, A. Petrone, T. Henderson, D. Ranasinghe, V. G. Zakrzewski, J. Gao, N. Rega, G. Zheng, W. Liang, M. Hada, M. Ehara, K. Toyota, R. Fukuda, J. Hasegawa, M. Ishida, T. Nakajima, Y. Honda, O. Kitao, H. Nakai, T. Vreven, K. Throssell, J. A. Montgomery Jr., J. E. Peralta, F. Ogliaro, M. J. Bearpark, J. J. Heyd, E. N. Brothers, K. N. Kudin, V. N. Staroverov, T. A. Keith, R. Kobayashi, J. Normand, K. Raghavachari, A. P. Rendell, J. C. Burant, S. S. Iyengar, J. Tomasi, M. Cossi, J. M. Millam, M. Klene, C. Adamo, R. Cammi, J. W. Ochterski, R. L. Martin, K. Morokuma, O. Farkas, J. B. Foresman and D. J. Fox, *Gaussian 16 Rev. C.01*, Wallingford, CT, 2016.
- 38 E. Aprà, E. J. Bylaska, W. A. de Jong, N. Govind, K. Kowalski, T. P. Straatsma, M. Valiev, H. J. J. van Dam, Y. Alexeev, J. Anchell, V. Anisimov, F. W. Aquino, R. Atta-Fynn, J. Autschbach, N. P. Bauman, J. C. Becca, D. E. Bernholdt, K. Bhaskaran-Nair, S. Bogatko, P. Borowski, J. Boschen, J. Brabec, A. Bruner, E. Cauët, Y. Chen, G. N. Chuev, C. J. Cramer, J. Daily, M. J. O. Deegan, T. H. Dunning, M. Dupuis, K. G. Dyall, G. I. Fann, S. A. Fischer, A. Fonari, H. Früchtl, L. Gagliardi, J. Garza, N. Gawande, S. Ghosh, K. Glaesemann, A. W. Götz, J. Hammond, V. Helms, E. D. Hermes, K. Hirao, S. Hirata, M. Jacquelin, L. Jensen, B. G. Johnson, H. Jónsson, R. A. Kendall, M. Klemm, R. Kobayashi, V. Konkov, S. Krishnamoorthy, M. Krishnan, Z. Lin, R. D. Lins, R. J. Littlefield, A. J. Logsdail, K. Lopata, W. Ma, A. V. Marenich, J. Del Martin Campo, D. Mejia-Rodriguez, J. E. Moore, J. M. Mullin, T. Nakajima, D. R. Nascimento, J. A. Nichols, P. J. Nichols, J. Nieplocha, A. Otero-de-la-Roza, B. Palmer, A. Panyala, T. Pirojsirikul, B. Peng, R. Peverati, J. Pittner, L. Pollack, R. M. Richard, P. Sadayappan, G. C. Schatz, W. A. Shelton, D. W. Silverstein, D. M. A. Smith, T. A. Soares, D. Song, M. Swart, H. L. Taylor, G. S. Thomas, V. Tipparaju, D. G. Truhlar, K. Tsemekhman, T. van Voorhis, Á. Vázquez-Mayagoitia, P. Verma, O. Villa, A. Vishnu, K. D. Vogiatzis, D. Wang, J. H. Weare, M. J. Williamson, T. L. Windus, K. Woliński, A. T. Wong, Q. Wu, C. Yang, Q. Yu, M. Zacharias, Z. Zhang, Y. Zhao and R. J. Harrison, *J. Chem. Phys.*, 2020, **152**, 184102.
- 39 J.-L. Brédas, D. Beljonne, V. Coropceanu and J. Cornil, *Chem. Rev.*, 2004, **104**, 4971–5004.
- 40 S. F. Nelsen, S. C. Blackstock and Y. Kim, *J. Am. Chem. Soc.*, 1987, **109**, 677–682.
- 41 M. C. Zerner, in *Reviews in computational chemistry*, ed. K. B. Lipkowitz and D. B. Boyd, VCH, New York, NY, 2007, pp. 313–365.
- 42 B. Baumeier, J. Kirkpatrick and D. Andrienko, *Phys. Chem. Chem. Phys.*, 2010, **12**, 11103–11113.
- 43 J. T. Kohn, N. Gildemeister, S. Grimme, D. Fazzi and A. Hansen, *J. Chem. Phys.*, 2023, **159**, 144106.
- 44 A. A. Hagberg, D. A. Schult and P. J. Swart, *Exploring network structure, dynamics, and function using NetworkX*, Pasadena, CA, USA, 2008.
- 45 R. A. Marcus, *Rev. Mod. Phys.*, 1993, **65**, 599–610.
- 46 Y. A. Berlin, G. R. Hutchison, P. Rempala, M. A. Ratner and J. Michl, *J. Phys. Chem. A*, 2003, **107**, 3970–3980.
- 47 S. Di Motta, E. Di Donato, F. Negri, G. Orlandi, D. Fazzi and C. Castiglioni, *J. Am. Chem. Soc.*, 2009, **131**, 6591–6598.
- 48 D. P. McMahon and A. Troisi, *J. Phys. Chem. Lett.*, 2010, **1**, 941–946.
- 49 J. E. Norton and J.-L. Brédas, *J. Am. Chem. Soc.*, 2008, **130**, 12377–12384.
- 50 (a) D. L. Cheung and A. Troisi, *Phys. Chem. Chem. Phys.*, 2008, **10**, 5941; (b) T. Xu, W. Wang and S. Yin, *J. Phys. Chem. A*, 2018, **122**, 8957–8964.
- 51 V. Rühle, A. Lukyanov, F. May, M. Schrader, T. Vehoff, J. Kirkpatrick, B. Baumeier and D. Andrienko, *J. Chem. Theory Comput.*, 2011, **7**, 3335–3345.
- 52 F. Neese, *Wiley Interdiscip. Rev.: Comput. Mol. Sci.*, 2022, **12**, e1606.
- 53 S. Grimme, S. Ehrlich and L. Goerigk, *J. Comput. Chem.*, 2011, **32**, 1456–1465.
- 54 S. Grimme, J. Antony, S. Ehrlich and H. Krieg, *J. Chem. Phys.*, 2010, **132**, 154104.
- 55 B. T. Thole, *Chem. Phys.*, 1981, **59**, 341–350.
- 56 (a) H. Berendsen, D. van der Spoel and R. van Drunen, *Comput. Phys. Commun.*, 1995, **91**, 43–56; (b) D. van der Spoel, E. Lindahl, B. Hess, G. Groenhof, A. E. Mark and H. J. C. Berendsen, *J. Comput. Chem.*, 2005, **26**, 1701–1718; (c) B. Hess, C. Kutzner, D. van der Spoel and E. Lindahl, *J. Chem. Theory Comput.*, 2008, **4**, 435–447; (d) S. Pronk, S. Páll, R. Schulz, P. Larsson, P. Bjelkmar, R. Apostolov, M. R. Shirts, J. C. Smith, P. M. Kasson, D. van der Spoel,



- B. Hess and E. Lindahl, *Bioinformatics*, 2013, **29**, 845–854; (e) M. J. Abraham, T. Murtola, R. Schulz, S. Páll, J. C. Smith, B. Hess and E. Lindahl, *SoftwareX*, 2015, **1–2**, 19–25.
- 57 W. L. Jorgensen, D. S. Maxwell and J. Tirado-Rives, *J. Am. Chem. Soc.*, 1996, **118**, 11225–11236.
- 58 G. A. Kaminski, R. A. Friesner, J. Tirado-Rives and W. L. Jorgensen, *J. Phys. Chem. B*, 2001, **105**, 6474–6487.
- 59 S. S. Skourtis, I. A. Balabin, T. Kawatsu and D. N. Beratan, *Proc. Natl. Acad. Sci. U. S. A.*, 2005, **102**, 3552–3557.
- 60 S. R. Marder, C. B. Gorman, F. Meyers, J. W. Perry, G. Bourhill, J. L. Brédas and B. M. Pierce, *Science*, 1994, **265**, 632–635.
- 61 R. Tomar, L. Bernasconi, D. Fazzi and T. Bredow, *J. Phys. Chem. A*, 2023, **127**, 9661–9671.
- 62 B. Le Guennic and D. Jacquemin, *Acc. Chem. Res.*, 2015, **48**, 530–537.
- 63 H. Lischka, D. Nachtigallova, A. J. A. Aquino, P. G. Szalay, F. Plasser, F. B. C. Machado and M. Barbatti, *Chem. Rev.*, 2018, **118**, 7293–7361.
- 64 C. Brückner and B. Engels, *Chem. Phys.*, 2017, **482**, 319–338.
- 65 T. Richards, M. Bird and H. Siringhaus, *J. Chem. Phys.*, 2008, **128**, 234905.
- 66 L. Stojanović, J. Coker, S. Giannini, G. Londi, A. S. Gertsen, J. Wenzel Andreasen, J. Yan, G. D'Avino, D. Beljonne, J. Nelson and J. Blumberger, *Phys. Rev. X*, 2024, **14**, 021021.
- 67 P. Friederich, F. Symalla, V. Meded, T. Neumann and W. Wenzel, *J. Chem. Theory Comput.*, 2014, **10**, 3720–3725.
- 68 G. D'Avino, L. Muccioli, F. Castet, C. Poelking, D. Andrienko, Z. G. Soos, J. Cornil and D. Beljonne, *J. Phys.: Condens. Matter*, 2016, **28**, 433002.
- 69 N. E. Jackson, K. L. Kohlstedt, L. X. Chen and M. A. Ratner, *J. Chem. Phys.*, 2016, **145**, 204102.
- 70 N. E. Jackson, L. X. Chen and M. A. Ratner, *Proc. Natl. Acad. Sci. U. S. A.*, 2016, **113**, 8595–8600.
- 71 T. Vehoff, B. Baumeier, A. Troisi and D. Andrienko, *J. Am. Chem. Soc.*, 2010, **132**, 11702–11708.
- 72 P. Friederich, V. Meded, A. Poschlad, T. Neumann, V. Rodin, V. Stehr, F. Symalla, D. Danilov, G. Lüdemann, R. F. Fink, I. Kondov, F. von Wrochem and W. Wenzel, *Adv. Funct. Mater.*, 2016, **26**, 5757–5763.
- 73 A. Troisi, A. Nitzan and M. A. Ratner, *J. Chem. Phys.*, 2003, **119**, 5782–5788.
- 74 D. N. Beratan, S. S. Skourtis, I. A. Balabin, A. Balaeff, S. Keinan, R. Venkatramani and D. Xiao, *Acc. Chem. Res.*, 2009, **42**, 1669–1678.
- 75 G. Schweicher, G. D'Avino, M. T. Ruggiero, D. J. Harkin, K. Broch, D. Venkateshvaran, G. Liu, A. Richard, C. Ruzié, J. Armstrong, A. R. Kennedy, K. Shankland, K. Takimiya, Y. H. Geerts, J. A. Zeitler, S. Fratini and H. Siringhaus, *Adv. Mater.*, 2019, **31**, 1902407.
- 76 A. Troisi, G. Orlandi and J. E. Anthony, *Chem. Mater.*, 2005, **17**, 5024–5031.
- 77 G. Ricci, S. Canola, Y. Dai, D. Fazzi and F. Negri, *Molecules*, 2021, **26**, 4119.
- 78 J. Spencer, F. Gajdos and J. Blumberger, *J. Chem. Phys.*, 2016, **145**, 064102.
- 79 A. Troisi, *Mol. Simul.*, 2006, **32**, 707–716.
- 80 S. Giannini, A. Carof and J. Blumberger, *J. Phys. Chem. Lett.*, 2018, **9**, 3116–3123.

